ADVANCED ELECTRONIC MATERIALS
www.advelectronicmat.de

Carbon-Enriched Amorphous Hydrogenated Boron Carbide Films for Very-Low-*k* Interlayer Dielectrics

*Bradley J. Nordell, Thuong D. Nguyen, Anthony N. Caruso, Sudhaunshu S. Purohit, Nathan A. Oyler, William A. Lanford, David W. Gidley, John T. Gaskins, Patrick E. Hopkins, Patrick Henry, Sean W. King, and Michelle M. Paquette**

A longstanding challenge in ultralarge-scale integration has been the continued improvement in low-dielectric-constant (low-*k*) interlayer dielectric materials and other specialized layers in back-end-of-the-line interconnect fabrication. Modeled after the success of carbon-containing organosilicate materials, carbon-enriched amorphous hydrogenated boron carbide (a-B_xC:H_y) films are grown by plasma-enhanced chemical vapor deposition from *ortho*-carborane and methane. These films contain more extraicosahedral sp^3 hydrocarbon groups than nonenriched a-B_xC:H_y films, as revealed by FTIR and NMR spectroscopy, and also exhibit lower dielectric constants than their nonenriched counterparts, notably due to low densities combined with a low distortion and orientation contribution to the total polarizability. Films with dielectric constant as low as 2.5 are reported with excellent electrical stability (leakage current of 10^{-9} A cm^{-2} at 2 MV cm^{-1} and breakdown voltage of >6 MV cm^{-1}), good thermal conductivity of 0.31 ± 0.03 W m^{-1} K^{-1}, and high projected Young's modulus of 12 ± 3 GPa. These properties rival those of leading SiOC:H materials, and position a-B_xC:H_y as an important complement to traditional Si-based materials to meet the complex needs of next-generation interconnect fabrication.

1. Introduction

As the microelectronics industry ventures into a nanoelectronics era, with half-pitch values reaching <10 nm, it faces challenges beyond mere component scaling. One of the most significant of these involves the back-end interconnect structures that support signal propagation between integrated circuit components. Specifically, inadequate signal speed, power consumption, and cross-talk metrics arising from conductor resistance (*R*) and dielectric capacitance (*C*) contributions are becoming major progress bottlenecks.[1,2] Aside from considering replacements for Cu as the conductor, the main thrust from a materials standpoint hinges on implementing novel low-dielectric-constant (low-*k*) materials, which include both the bulk interlayer dielectric (ILD) and specialized low-*k* layers such as etch stops and diffusion barriers.[3] However, because candidate materials must not only meet *k* requirements, but also a laundry list of additional chemical, thermal, electrical, and mechanical integration metrics, finding suitable low-*k* alternatives has been extremely challenging.

Although many classes of materials have been proposed as candidate low-*k* solutions, the semiconductor industry has not ventured far from its roots. In 2001, the original interlayer dielectric material, SiO_2 ($k \approx 4.1$), was replaced by a carbon-containing variant, SiOC:H ($k \approx 3.0$). Fifteen years later, despite the original goals set forth by the International Technology Roadmap for Semiconductors of achieving *k* values of <2 by 2012, the industry is still using porous SiOC:H variants with *k* values of only 2.55.[4] One of the reasons this materials science problem has proven so challenging is because the very low densities required to

B. J. Nordell, T. D. Nguyen, Prof. A. N. Caruso, Prof. M. M. Paquette
Department of Physics and Astronomy
University of Missouri-Kansas City
Kansas City, MO 64110, USA
E-mail: paquettem@umkc.edu

S. S. Purohit, Prof. N. A. Oyler
Department of Chemistry
University of Missouri-Kansas City
Kansas City, MO 64110, USA

Prof. W. A. Lanford
Department of Physics
University at Albany
Albany, NY 12222, USA

Prof. D. W. Gidley
Department of Physics
University of Michigan
Ann Arbor, MI 48109, USA

Dr. J. T. Gaskins, Prof. P. E. Hopkins
Department of Mechanical and Aerospace Engineering
University of Virginia
Charlottesville, VA 22904, USA

Dr. P. Henry, Dr. S. W. King
Logic Technology Development
Intel Corporation
Hillsboro, OR 97124, USA

DOI: 10.1002/aelm.201700116

 © 2017 WILEY-VCH Verlag GmbH & Co. KGaA, Weinheim

achieve targeted k values inevitably lead to a dramatic falloff in chemical and mechanical stability.[5] While some researchers continue to explore novel materials such as metal–organic frameworks[6] to address this issue, the industry has turned to more exotic strategies to strengthen very-low-k solids, including designer backbone engineering[7] and pore stuffing.[8,9]

Beyond the basic low-density requirement, the ideal constitutional framework for a low-k or low-permittivity material is a covalent low-Z (Z = atomic number) solid. Of the possible classes of materials not based on Si, a large amount of research has been dedicated to carbon-based solids, but these have never managed to make significant inroads.[4] Another seemingly obvious class of materials with potential for low-k applications, which has received minimal consideration, comprises the boron-rich solids. We recently reported a class of low-k carborane-based amorphous hydrogenated boron carbide (a-B_xC:H_y) films with markedly superior mechanical properties relative to Si-based dielectrics.[10] For these films, however, optimal chemical and electrical stability were only obtained in a moderate k range of 3.0–3.5. While this combination of properties is ideal for low-k etch stop or diffusion barrier applications, lower k values are needed for bulk interlayer dielectric applications.

Based on the historical success of carbon incorporation into silicon oxides, we hypothesized that the addition of carbon to a-B_xC:H_y films might likewise lead to similar benefits. Herein we describe carbon-enriched a-B_xC:H_y films, grown by plasma-enhanced chemical vapor deposition (PECVD) using the solid-state molecular precursor *ortho*-carborane ($C_2B_{10}H_{12}$) and methane as an additional carbon source, with k values as low as 2.5 and an average Young's modulus of 12 ± 3 GPa, mechanically superior to the overwhelming majority of SiCO:H films within a similar k range and on par with the best designer SiCO:H films reported to date.[7,11] With good performance for a number of additional integration properties, including leakage current of 10^{-9} A cm^{-2} at 2 MV cm^{-1}, breakdown voltage of >6 MV cm^{-1}, and thermal conductivity of 0.31 ± 0.03 W m^{-1} K^{-1}, these a-B_xC:H_y films make excellent candidates for next-generation low-k applications.

2. Results and Discussion

2.1. Chemical Composition and Local Physical Structure

Several series of carbon-enriched amorphous hydrogenated boron carbide (a-B_xC:H_y) films were grown by plasma-enhanced chemical vapor deposition from *ortho*-carborane and methane, with base conditions chosen from among those known to produce a-B_xC:H_y films with desirable low-k dielectric properties.[10] For each series, the %CH_4 was varied within a range of 2.5% and 50%. The growth conditions for the films, as well as for control films grown without the addition of methane, are summarized in **Table 1**, alongside a number of measured properties.

With the addition of CH_4 as a reactive plasma gas, the carbon content of the a-B_xC:H_y films increases significantly, which corresponds to a decrease in the B/C ratio (**Figure 1**). The atomic concentration of hydrogen tracks the carbon content, suggesting that carbon is being incorporated in the form of hydrocarbon, CH_n. Finally, the increase in carbon is associated with a decrease in density, which suggests that the additional hydrocarbon contributes to increased free volume within the films.

It is noteworthy that the atomic concentration of oxygen measured within the films was relatively high (9% on average for the carbon-enriched films grown in this study) compared to previously grown pure carborane-based films (4% on average[12,13]). We might have predicted the opposite result owing to the expected hydrophobicity of the hydrocarbon-rich films.[14] The oxygen may, however, have originated from the methane gas itself (99.99%), despite our efforts to purify to ppb level with O_2 and H_2O filters. We have found in previous work that the purity of the process gas is extremely important in minimizing oxygen, and that transitioning from Ar with <100 ppb O_2/H_2O to Ar with <1 ppb O_2/H_2O allowed for average oxygen levels in the a-B_xC:H_y films to be reduced from 10–15% to <5%.[12,15] The higher oxygen concentration could also have originated from postgrowth atmospheric oxidation as a result of the lower density and increased porosity in these films. Oxygen concentration does show a correlation with density (albeit weak, with R^2 = 0.4), and the two films with higher than expected porosity (Q14 and R7, vide infra) both show higher than average oxygen content for their specific density.

Amorphous hydrogenated boron carbide films grown from pure *ortho*-carborane are hypothesized to be made up of carborane molecules cross-linked either directly to each other or via extraicosahedral hydrocarbon linking groups, with varying degrees of cross-linking and hydrogen saturation.[12,16] To gain a better understanding of the chemical nature of the added carbon within these films, we performed FTIR and solid-state NMR analysis on a series of samples grown with varying partial flow rates of methane. In **Figure 2**a, we contrast the FTIR spectrum of a film grown with no methane to those of films grown with 5%, 10%, 25%, and 50% CH_4. The spectra can be divided into three regions: (A) the C—H stretch region (2800–3200 cm^{-1}), (B) the B—H stretch region (≈2600 cm^{-1}),[17] and (C) the region <1500 cm^{-1}, which includes icosahedral vibration modes and a number of other modes (C—B stretch, CH_n bending and rocking, etc.).

In the C—H stretch region (Figure 2b), the peak at ≈3070 cm^{-1} is assigned to the intraicosahedral C—H group within the carborane molecule,[18] and is the dominant peak for the film grown without added CH_4. Peaks between 2800 and 3000 cm^{-1} are assigned to extraicosahedral hydrocarbon sp^3 C—H stretching modes. With the addition of only 5% CH_4, the intensity of the peaks in this region increases significantly relative to that of the peak at 3070 cm^{-1}, going from an ≈1:1 ratio between extraicosahedral:intraicosahedral C—H peaks to an ≈3:1 ratio (**Figure 3**), thus corroborating a substantial increase in extraicosahedral hydrocarbon. As methane is added to the plasma in greater proportions, these peaks become even more dominant, with the extraicosahedral:intraicosahedral C—H peak ratio reaching ≈5:1 for the film grown with 50% CH_4.

For the carbon-rich films grown with 5–10% CH_4, four main peaks can be observed in the extraicosahedral C—H stretch region at ≈2955, 2905, 2875, and 2835 cm^{-1}, with the spectral envelope in the 2800–3000 cm^{-1} range being fairly similar to that for the films grown with no added CH_4. For the films

© 2017 WILEY-VCH Verlag GmbH & Co. KGaA, Weinheim

Table 1. Process parameters and properties for carbon-enriched a-B_xC:H_y films compared to their nonenriched counterparts.

Film no.	Temp [°C]	Power [W]	Pressure [Torr]	Total flow [sccm]	Partial flow [sccm]	CH_4 flow [sccm]	d [nm]	B/C	At% B	At% C	At% O	At% H	D [g cm^{-3}]	Pore size [nm]	E [GPa]	H [GPa]	ε_1 [a)]	k [a)]	k–ε_1	ρ [Ω cm]	J@2 MV cm^{-1} [b)] [A cm^{-2}]	λ [W m^{-1} K^{-1}]
R0	250	10	0.4	100	90	10	566	2.5	32.3	12.7	7.3	47.7	1.17	–	12.1 (±1.4)	0.71 (±0.04)	2.7	3.1	0.4	4×10^{13}	4×10^{-6}	0.28 (±0.03)
R1	250	10	0.4	100	50	50	381	3.9	39.0	10.1	5.5	45.4	1.20	–	9.3 (±0.7)	0.57 (±0.04)	2.5	3.3	0.8	4×10^{13}	2×10^{-6}	0.29 (±0.03)
Q33 [c)]	250	10	0.4	100	100	0	152	– [d)]	–	–	–	–	–	–	–	–	2.9	3.2	0.3	1×10^{14}	2×10^{-7}	–
R2	250	40	2	100	90	10	192	1.3	25.2	18.8	10.3	45.7	1.22	–	7.7 (±2.1)	0.70 (±0.07)	2.4	2.8	0.4	1×10^{14}	1×10^{-7}	0.31 (±0.04)
Q14	250	40	2	100	100	0	60	4.1	50.1	12.2	6.0	31.6	1.63	0.79 (±0.04)	34 (±2)	4.1 (±0.3)	3.5	3.7	0.2	4×10^{13}	8×10^{-8}	–
R3	250	40	2	200	180	20	213	0.9	19.9	22.6	7.0	50.5	1.15	0.69 (±0.03)	15.5 (±2.7)	0.78 (±0.06)	2.4	2.7	0.3	4×10^{13}	1×10^{-7}	0.29 (±0.04)
R4	250	40	2	200	150	50	436	0.7	17.2	23.6	4.9	54.3	1.18	0.63 (±0.03)	12.0 (±1.5)	0.49 (±0.02)	2.5	3.1	0.6	3×10^{13}	4×10^{-9}	0.29 (±0.03)
R5	250	40	2	200	100	100	466	0.8	25.6	31.4	4.6	38.4	1.13	–	12.9 (±0.5)	0.67 (±0.04)	2.5	3.5	1.0	3×10^{13}	1×10^{-8}	0.29 (±0.03)
R6	275	40	2	200	195	5	149	2.1	35.0	17.0	3.4	44.6	1.29	–	–	–	2.7	3.0	0.3	5×10^{13}	7×10^{-8}	–
R12 [e)]	275	40	2	200	180	20	110	–	–	–	–	–	–	–	–	–	2.8	–	–	–	–	–
Q32 [c)]	275	40	2	200	200	0	200	4.7	46.9	10.2	5.5	37.5	1.44	[f)]	126 (±4)	8.6 (±0.04)	3.0	3.3	0.3	5×10^{14}	5×10^{-9}	0.49 (±0.04)
R7	275	20	2	200	195	5	583	3.8	33.8	8.8	15.6	41.8	1.12	0.62 (±0.01) 2.02 (±0.04)	–	–	2.4	2.7	0.3	1×10^{13}	3×10^{-7}	–
R11	275	20	2	200	190	10	244	1.6	29.1	17.9	9.8	43.1	0.91	0.71 (±0.01)	–	–	2.2	2.5	0.3	1×10^{14}	2×10^{-9}	0.31 (±0.03)
R13	275	20	2	200	200	0	176	2.9	36.1	12.4	8.2	43.3	1.29	0.54 (±0.01)	–	–	2.7	3.0	0.3	3×10^{13}	4×10^{-8}	0.50 (±0.04)
R8	175	20	2	200	195	5	523	3.4	34.0	10.0	11.6	44.4	1.08	–	–	–	2.2	2.5	0.3	1×10^{14}	1×10^{-9}	–
R10	400	10	0.4	100	90	10	510	2.5	33.2	13.1	13.6	40.1	0.84	–	–	–	2.7	3.2	0.5	–	3×10^{-6}	–
R9	400	10	0.4	100	50	50	150	1.6	24.7	15.9	13.6	45.8	0.98	–	–	–	2.4	2.8	0.4	–	–	–
Q11 [c)]	400	10	0.4	100	100	0	844	4.9	49.2	10.0	4.0	36.9	1.51	[f)]	–	–	3.4	4.0	0.6	4×10^{15}	2×10^{-7}	–

[a)]Variability on the order of 0.15 (ref. [10]); [b)]Variability on the order of 5×10^{-9} A cm^{-2} (ref. [10]); [c)]Ref. [10]; [d)]Dash indicates film was not measured; [e)]Delaminated prior to measurement; [f)]Positronium intensity <2%.

© 2017 WILEY-VCH Verlag GmbH & Co. KGaA, Weinheim

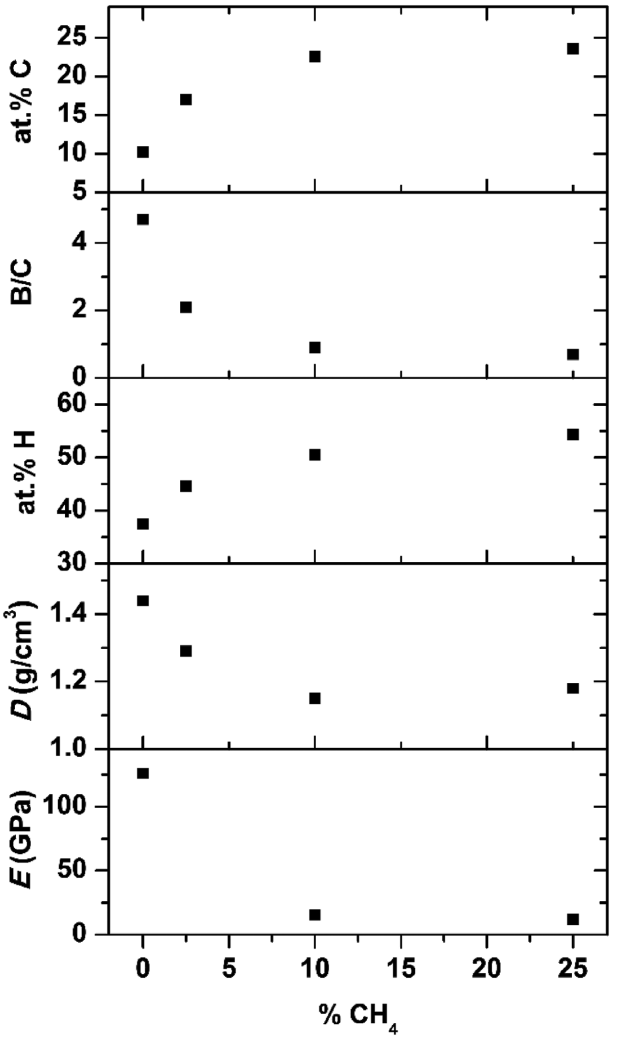

Figure 1. Chemical composition (at% C, B/C, and at% H), density (*D*), and Young's modulus (*E*) as a function of partial methane flow rate (0%, 2.5%, 10%, and 25%) for a-$B_xC:H_y$ films grown at 250/275 °C, 40 W, 2 Torr, and 200 sccm total flow rate.

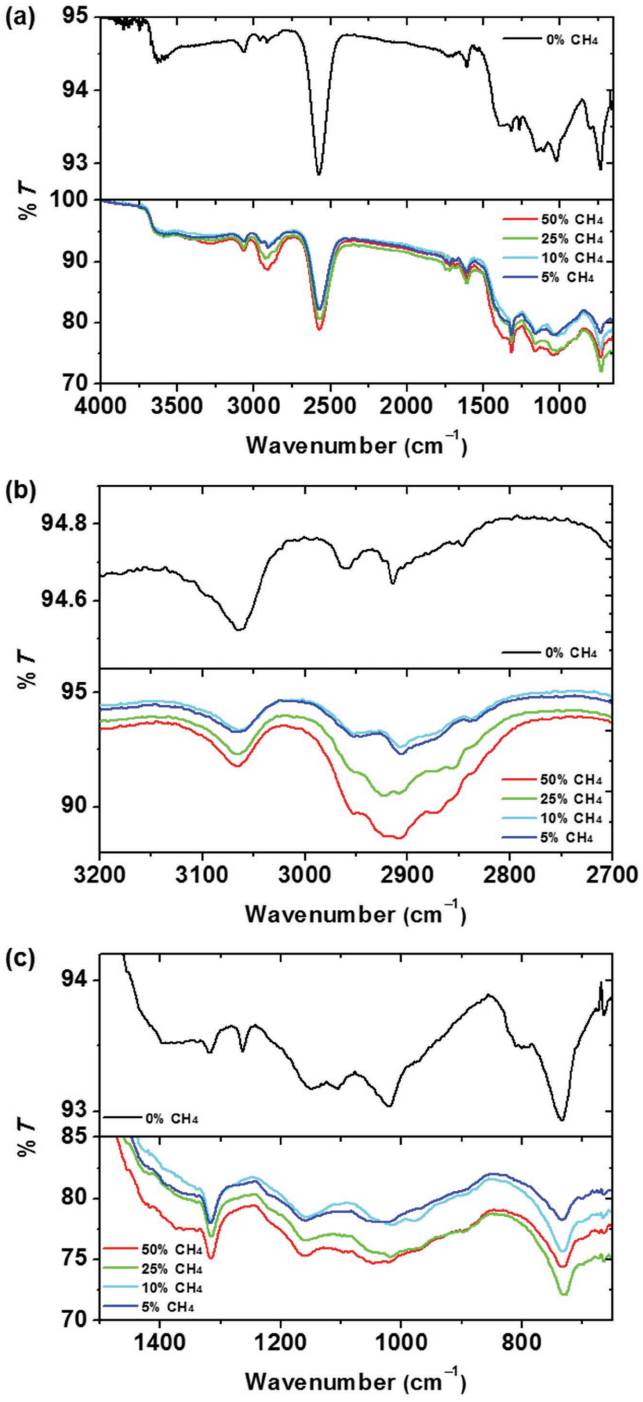

Figure 2. FTIR spectra of a-$B_xC:H_y$ films grown at 250 °C, 40 W, 2 Torr, and 200 sccm total flow rate with varying partial CH_4 flow rates (0%, 5%, 10%, 25%, and 50%), including a) the full spectrum and b) expansions of the C—H stretch region and c) the <1500 cm^{-1} region.

grown with 25–50% CH_4, two additional peaks clearly appear at ≈2920 and 2850 cm^{-1}. The identity of the hydrocarbon peaks within the 2800—3000 cm^{-1} region is generally well-established, with typical assignments being the sp^3 CH_3 asymmetric and symmetric stretches at ≈2950 and 2870 cm^{-1}, respectively, and the sp^3 CH_2 asymmetric and symmetric stretches at ≈2920 and 2850 cm^{-1}, respectively.[19–21] In the carbon-rich films grown with 25–50% added methane, we distinctly observe all of these peaks, and thus tentatively assign them to the standard functional groups. It is noteworthy that the peaks assigned to the CH_2 stretches are absent for the films grown with 5–10% added methane. The origin of the peaks at 2905 and 2835 cm^{-1}, which are observed in all of the spectra, is not clear. One possibility is that these represent the asymmetric and symmetric sp^3 CH_2 stretches for bridging CH_2 bound—not to carbon—but rather to boron. Such an interpretation would imply that films containing lower amounts of extraicosahedral hydrocarbon would predominantly exhibit B—CH_2—B linkages, but those containing higher amounts of extraicosahedral hydrocarbon would exhibit a greater amount of the C—CH_2—C type of linkages traditionally found in carbon-based materials.

To obtain a more quantitative idea of the changes within the C—H stretch region, the spectra were deconvoluted using Lorentzian functions after subtracting a linear baseline, as

© 2017 WILEY-VCH Verlag GmbH & Co. KGaA, Weinheim

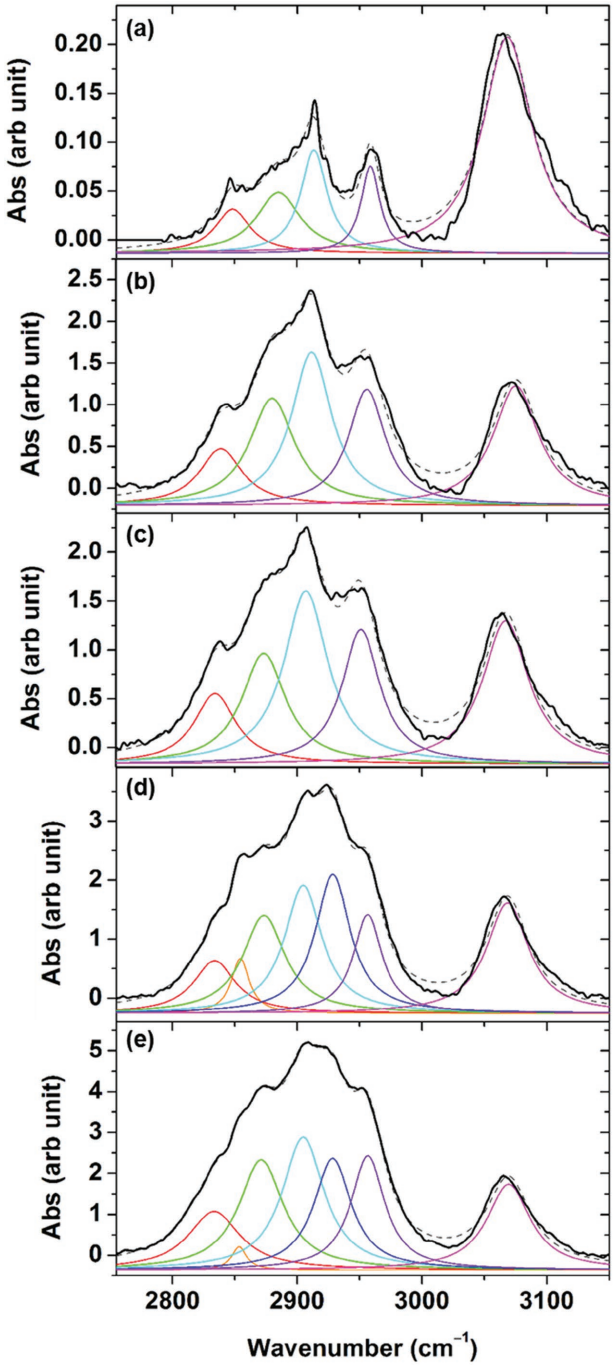

Figure 3. Deconvolution of the FTIR spectra of a-B_xC:H_y films in the C—H stretch region from 2755 to 3150 cm^{-1} for films grown with a) 0%, b) 5%, c) 10%, d) 25%, and e) 50% partial CH_4 flow rate. Colored lines represent fitted peaks, dashed gray lines represent the summation of the fitted peaks, and black lines represent the original data.

shown in Figure 3. For all of the spectra, the intraicosahedral C—H peak at ≈3070 cm^{-1} was fit to one peak. For the spectra of films grown with 0–10% CH_4, the extraicosahedral C—H stretch region was best fit to four peaks. For the spectra of films grown with 25–50% CH_4, six peaks are clearly visible, and six peaks yielded a good fit. We note that it is likely that, due to the complex chemical structure of the material, there are more than four or six chemical environments for C—H bonds in the solid (e.g., B—CH_2—C in addition to C—CH_2—C and B—CH_2—B, or CH_3 bound to B in addition to CH_3 bound to C); however, we prefer to consistently fit fewer peaks that may represent more than one unique type of environment than to inconsistently fit too many hypothetical peaks. The key observations from the deconvolution are as follows. First, the peak clearly visible at ≈2850 cm^{-1} in the carbon-rich films apparently represents a minor contribution to the total intensity, despite it appearing quite sharp, particularly for the spectrum of the film grown with 25% CH_4 (Figure 3d). Second, both of the peaks that appear in the spectra for the carbon-rich films (≈2920 and 2850 cm^{-1}), that we assign to sp^3 CH_2 asymmetric and symmetric stretches, respectively, increase in intensity for the film grown at 25% CH_4, but decrease in intensity for the film grown at 50% CH_4. By contrast, all of the other peaks in the spectra continually increase in intensity relative to the intraicosahedral C—H peak at 3070 cm^{-1} with the addition of increasing CH_4. This could indicate that, as the films become more carbon-rich, bridging C—CH_2—C species are initially formed at lower C concentrations, but that higher amounts of CH_3 groups are formed at the highest C concentrations. This interpretation would be consistent with the behavior observed in SiC_x:H films.[22,23]

The region <1500 cm^{-1} (Figure 2c) contains methyl and methylene bending modes in the range of 1250–1500 cm^{-1} and primarily icosahedron-based vibrational modes at <1200 cm^{-1}.[18] The most significant change in this region is an increase in intensity of a sharp peak at 1315 cm^{-1} accompanied by the disappearance of a peak at 1265 cm^{-1} in the more carbon-rich films. Common assignments for sp^3 CH_2/CH_3 bending modes in hydrocarbons are sp^3 CH_3 asymmetric and symmetric bending modes at ≈1470 and 1380 cm^{-1}, respectively, and sp^3 CH_2 bending modes at 1465 and 1300 cm^{-1}.[21] Although we cannot definitively identify the peak at 1315 cm^{-1} because the energies (and intensities) of the vibrational modes depend strongly on chemical environment, we tentatively assign this peak to an sp^3 CH_2 bend after Stuart.[21] This assignment is supported by the typical identification of the CH_2 bending mode for bridging Si—CH_2—Si groups in organosilicate glasses at a slightly higher wavenumber of ≈1350 cm^{-1},[22,24] although again, a direct comparison cannot be made due to the differences between Si and B chemical environments. A number of changes are additionally observed in the region <1200 cm^{-1}; however, the spectra are complex and it is therefore difficult to draw any definitive conclusions from this information. The literature on a-BC:H is generally inconsistent[25–27] and does not discuss the identification of hydrocarbons in this region per se. It is, however, possible that some of the weak peaks that appear for the methane-enriched films (e.g., at ≈900 and 750 cm^{-1}) represent CH_3 rocking modes, as these are typically observed in the 700–900 cm^{-1} region for organosilicates.[22,24]

Similarly to the FTIR spectra, the solid-state NMR spectra reveal a clear increase in extraicosahedral hydrocarbon for films grown with added CH_4 (**Figure 4**). Two major peaks in the ^{13}C NMR spectrum have been previously assigned to intraicosahedral hydrogenated carbon (≈60 ppm) and extraicosahedral carbon (≈0 ppm).[16] When no CH_4 is added, the intraicosahedral C peak dominates, with a ≈2:1 area ratio, relative to the

 © 2017 WILEY-VCH Verlag GmbH & Co. KGaA, Weinheim

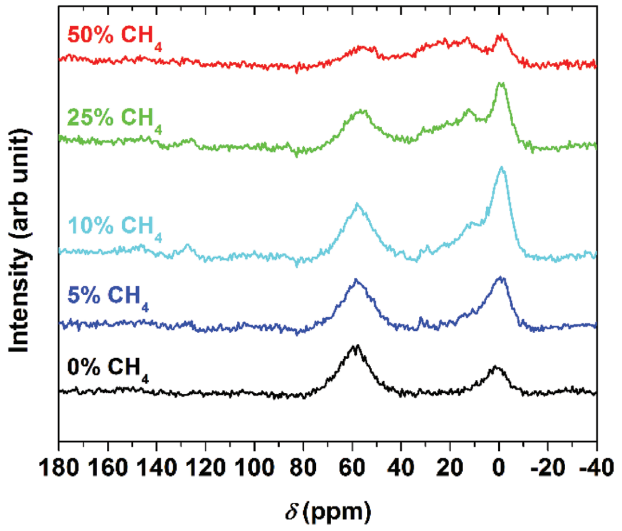

Figure 4. ^{13}C solid-state NMR spectra of a-B_xC:H_y films grown at 250 °C, 40 W, 2 Torr, and 200 sccm total flow rate with varying partial CH_4 flow rates.

extraicosahedral region (–10 to 40 ppm). Upon addition of 5% CH_4, the two regions exhibit closer to a 1:1 area ratio, and the relative intensity of the extraicosahedral hydrocarbon-based region continues to increase with increasing CH_4. Further, with increasing CH_4, the appearance of the extraicosahedral hydrocarbon region changes. First, a peak at ≈12 ppm becomes particularly clear for films grown with 10% and 25% CH_4, and second, a broad feature spanning ≈20–40 ppm becomes more pronounced, and is especially evident in the film grown with 50% CH_4. Although we can confidently state that peaks in this region originate from sp^3 hydrocarbon, peak assignments are still tentative. Based on our previous work, in which we calculated the ^{13}C chemical shifts of various carborane molecular clusters,[16] the dominant peak at ≈0 ppm can be assigned to CH_n groups bound to carborane cages via boron (B—CH_2—B, B—CH_3, or $(B)_3$—CH). The peak at ≈12 ppm can be assigned to a CH_3 group bound to carbon rather than boron (C—CH_3) or a CH_2 group bound to only one boron atom (C—CH_2—B). Spectral intensity in the 20–40 ppm range likely indicates CH_2 or possibly CH groups bound entirely to carbon.[28,29] Finally, a weak peak at ≈130 ppm in the carbon-enriched films suggests the presence of some sp^2-based carbon.[28,29] Overall, the NMR data suggest that with carbon enrichment of the a-B_xC:H_y films, we are seeing, in addition to increased extraicosahedral CH_n in general, a shift from CH_n groups bound to boron toward CH_n groups bound to carbon.

The porosity of a subset of the films was investigated using positron annihilation lifetime spectroscopy (PALS). The carbon-enriched films were found to have pore sizes in the range of 0.6–0.7 nm, consistent with previous studies on pure carborane-based a-B_xC:H_y films, which revealed that lower density films (<1.5 g cm^{-3}) exhibited pore diameters in this same range,[12,13] and that the *IV* product (positronium signal intensity × pore volume) yielded a general inverse correlation with thin-film density. Here, too, *IV* product generally tracks thin-film density: film R13 with a density of 1.29 g cm^{-3} has the lowest *IV* value of 0.67% nm^3 and film R11 with a density of 0.91 g cm^{-3} has the highest *IV* value of 1.77% nm^3, while films R3 and R4 with densities of 1.15 and 1.18 g cm^{-3} in the middle of this range have *IV* values of 1.42% and 0.89% nm^3, respectively. In the case of R3 and R4, where the densities are approximately the same but the *IV* values differ, the higher *IV* value is correlated with a lower *k* value. Two unusual PALS results can be noted in Table 1. First, film R7 exhibits an atypical bimodal pore distribution. The reason for this is unclear, although we note that this film also exhibits an unexpectedly low carbon content and high oxygen content, which may suggest an unusual composition/structure. Second, film Q14 exhibits an unexpectedly high pore diameter (0.79 nm) and high *IV* product (0.82) for a high-density film (1.63 g cm^{-3}). Film Q14 also has an unexpectedly low Young's modulus (we would expect it to be in the range of 150–200 GPa for a film of this density based on trends compiled from dozens of similar films),[10] which may likewise suggest that this film also possesses an unusual composition/structure.

2.2. Dielectric Properties

Perhaps of greatest interest to the current study is the effect of added carbon on the dielectric properties of the a-B_xC:H_y films. The "dielectric constant," *k*, equivalent to the relative permittivity, ε_r, relates to the polarizability of a material in the presence of an electric field. This is a frequency-dependent property that can be broken down into different mechanisms that operate over different frequency ranges: (1) electronic polarization (displacement of the electron cloud) occurs at high (optical) frequencies, (2) distortion polarization (vibration of bonds) occurs at moderate (infrared) frequencies, and (3) orientation polarization (movement of permanent dipoles) occurs at low (microwave/radiowave) frequencies. The low-frequency response encompasses all three polarization mechanisms. We have measured both high-frequency (10^{14} Hz) dielectric constant (referred to here as ε_1) and low-frequency (10^5 Hz) dielectric constant (referred to here as *k*), where the low-frequency measurement is taken as the total dielectric constant and thus represents the sum of all three contributions. The difference between the two measurements, $k - \varepsilon_1$, thus represents the sum of distortion and orientation polarization contributions.[30,31]

We find that films grown with added CH_4 generally tend to exhibit lower dielectric constants than those grown without. However, the relationship between the partial flow rate of CH_4 (and consequently total at% C) and the dielectric constant is not necessarily smooth, as is evident from **Figure 5**, which summarizes changes in *k*, ε_1, and $k - \varepsilon_1$ for a series of carbon-enriched films. Here, we see that ε_1 decreases to 2.4–2.5 for films grown with ≥10% CH_4 (Figure 5a). However, while *k* decreases to a minimum value of 2.7 at 10% CH_4, it increases again with higher flow rates of CH_4, indicating that the $k - \varepsilon_1$ contribution does not necessarily track with ε_1, but rather increases for the films grown with the highest methane flows (Figure 5b). Because the ε_1 term represents the electronic polarization contribution, we expect it to depend on the total electron density of the material, and thus decrease as a function of lower-*Z* constituents and lower atom density. Since B and C have comparable

© 2017 WILEY-VCH Verlag GmbH & Co. KGaA, Weinheim

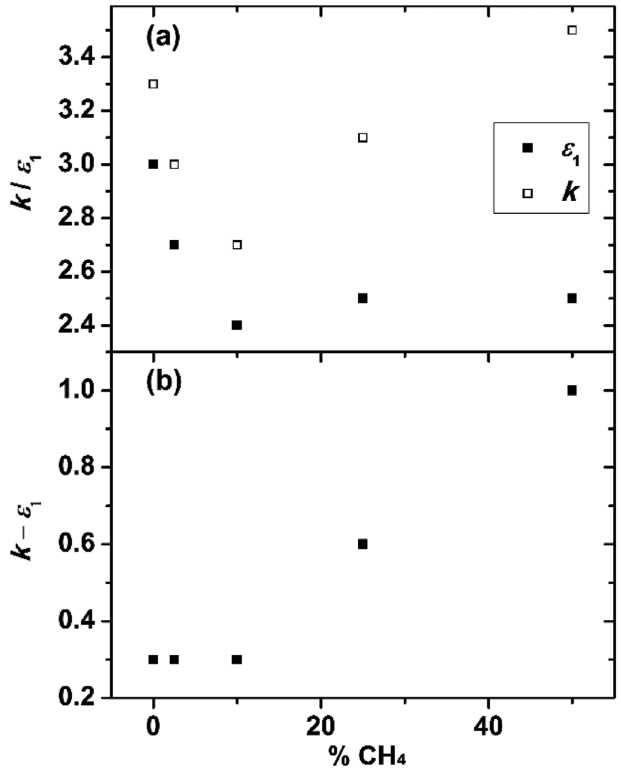

Figure 5. a) High-frequency (ε_1) and low-frequency (total, k) dielectric constant as well as b) the difference between the two ($k - \varepsilon_1$) for a-B_xC:H_y films grown at 250/275 °C, 40 W, 2 Torr, and 200 sccm total flow rate with varying CH_4 partial flow rates.

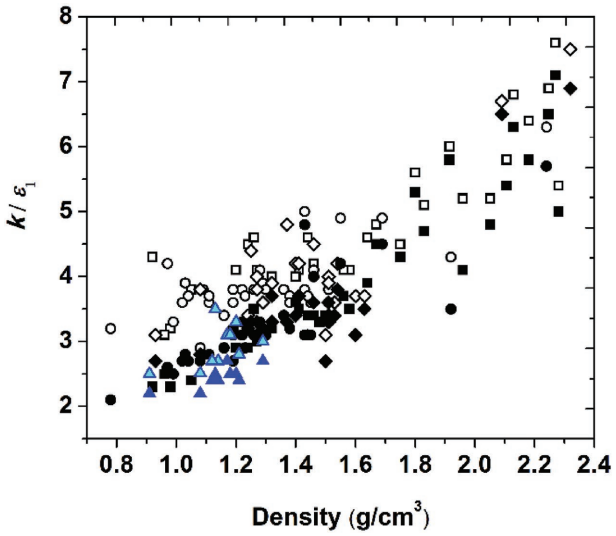

Figure 6. High- (ε_1, 4.6 × 10^{14} Hz/1.96 eV, open symbols) and low- (k, 100 kHz, closed symbols) frequency dielectric constants as a function of density for carbon-enriched (blue triangle symbols) versus nonenriched (black symbols) amorphous hydrogenated boron carbide films (■/□ = ref. [12], ●/○ = ref. [13], ♦/◇ = ref. [10], ▲/△ = this work).

electron densities (and in fact B has a lower atomic number than C), we would not expect an increase in C per se to lead to a decrease in ε_1. However, we would expect the increase in at% H and decrease in atomic density associated with increasing at% C to lead to a decrease in ε_1. Indeed, the observed change in ε_1 closely mirrors the observed changes in at% H and density for these films (see Figure 1). The $k - \varepsilon_1$ term represents the sum of ionic and orientation polarization contributions. We might predict these contributions to increase due to an increase in polar oxygen-based bonds (e.g., OH); however, we find no significant correlation between at% O and the magnitude of the $k - \varepsilon_1$ term. In a previous publication,[10] we discussed the proposed existence of a rigidity transition in a-B_xC:H_y films, where below a given density (≈1.3 g cm^{-3}), the film transitions from an overconstrained "rigid" to an underconstrained "floppy" solid.[32,33] Because the "floppy" network has a much greater number of flexible modes, one might expect this to lead to greater distortion and/or orientation polarization.[34] It may be the case that for films with moderate carbon enrichment (2.5–10% CH_4), the density of the a-B_xC:H_y films can decrease below 1.3 g cm^{-3} without a loss of rigidity due to the incorporation of network-rigidifying CH_2 bridging groups (vs one-fold-coordinate terminal hydrogen atoms), but for films with higher carbon enrichment (25–50% CH_4), a greater increase in terminal CH_3 groups again leads to underconstrained "floppy" films, consequently leading to higher $k - \varepsilon_1$ values in the case of the highest-C-content films despite their low density. The importance of the type of carbon bonding in organosilicates (e.g., Si—CH_3 vs Si—CH_2—Si) has been routinely emphasized in the context of enhancing mechanical strength for this class of materials;[11] in amorphous boron carbide, the carbon bonding may also play an important role in optimizing the dielectric properties.

Importantly, we have previously found that for pure carborane-based a-B_xC:H_y films, below densities of ≈1.5 g cm^{-3}, $k - \varepsilon_1$ tended to be quite high.[10] Thus even if very low ε_1 values (<2.5) could be achieved for low-density films, k inevitably remained relatively high (>3), with the lowest measured value of k being 2.7 and the lowest average values being ≈3.0. With the addition of CH_4, we are able to achieve not only lower ε_1 values for low-density films, but also significantly lower $k - \varepsilon_1$ values, and thus achieve much lower overall k values. This result is compellingly illustrated in **Figure 6**, which contrasts ε_1 and k values as a function of density for carbon-enriched and nonenriched a-B_xC:H_y films. By enriching carborane-based a-B_xC:H_y films with CH_4, we are able to consistently obtain films with k < 3.0 and as low as 2.5.

2.3. Mechanical, Electrical, and Thermal Properties

As we have repeatedly emphasized in our work, obtaining low-k values alone is not the goal, as a number of other properties are critical for dielectric integration. One of these properties is mechanical stability, for which Young's modulus (E) is the most commonly compared metric. Carborane-based a-B_xC:H_y films have been previously demonstrated to exhibit extremely high Young's modulus for a given k value, significantly higher than for traditional Si-based dielectrics.[10] For films with k in the range of ≈3.5–7.5, E was found to track linearly with k in the range of ≈100–400 GPa. Importantly, even for low-density films where E might be predicted to fall off dramatically with density, the Young's modulus was observed to plateau at

© 2017 WILEY-VCH Verlag GmbH & Co. KGaA, Weinheim

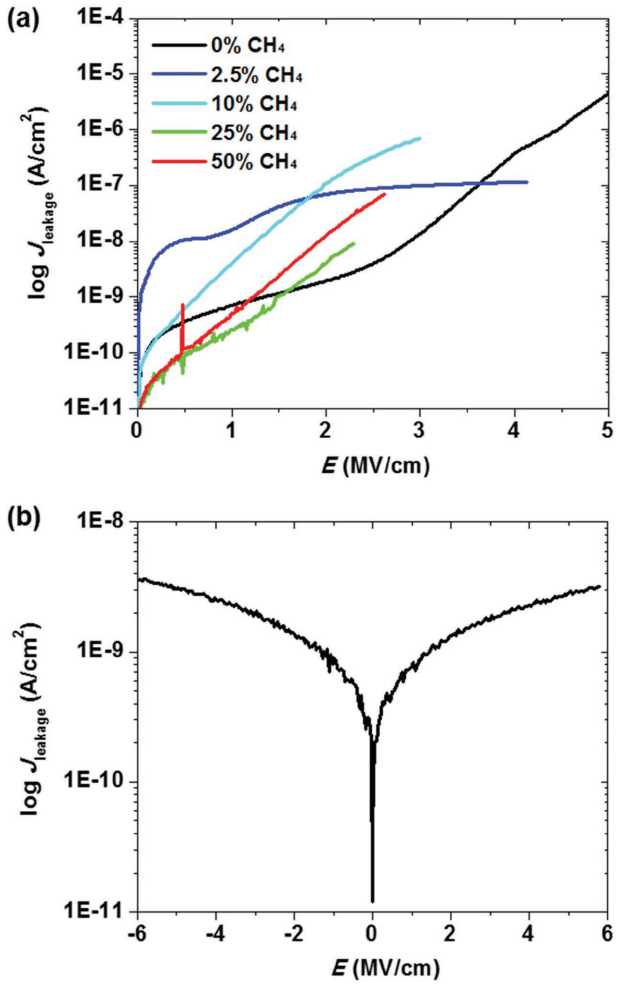

Figure 7. a) Leakage current traces for a series of a-$B_xC:H_y$ films grown at 250/275 °C, 40 W, 2 Torr, and 200 sccm total flow rate with varying CH_4 partial flow rates (note that the limits of the *J*–*E* curves do not represent breakdown but rather the highest electric field that could be applied for a given thickness of film). b) Forward and reverse bias *J*–*E* curves for a-$B_xC:H_y$ film R11 demonstrating leakage current of 2×10^{-9} A cm^{-2} at 2 MV cm^{-1} and breakdown voltage of ≥6 MV cm^{-1}.

a relatively high value of 21 ± 9 GPa for films with densities in the range of 0.9–1.2 g cm^{-3}. For the carbon-enriched films, the Young's modulus values were found to be lower than for their nonenriched counterparts (Table 1), which is unsurprising given the substitution of extremely strong boron-based bonds with carbon-based bonds. However, they still exhibit a high average value of 12 ± 3 GPa for films with densities in the range of 1.1–1.2 g cm^{-3}, and we can extrapolate that this value would hold for films with densities in the range of 0.9–1.1 g cm^{-3} based on trends observed in the nonenriched films. For very-low-*k* films with *k* in the range of 2.5–3.0, this represents a Young's modulus higher than the majority of SiOC:H films, and on par with the best designer films reported to date.[7,11]

One of the deficiencies found in pure carborane-based a-$B_xC:H_y$ films was that the lowest-density films tended to exhibit high leakage currents or low breakdown voltages relative to moderate-density films.[10] Through the addition of methane, we are able to consistently grow lower-density, lower-*k* films with excellent electrical properties. In **Figure 7**a, we show leakage current traces for a series of films grown with similar conditions and varying flow rates of CH_4. It is evident that the carbon-enriched films—three out of four of which have lower *k* values that the analogous nonenriched film—possess leakage current values on the order of 10^{-8} A cm^{-2} or lower at 2 MV cm^{-1}. The lowest-*k* films grown (*k* = 2.5), R8 and R11, both demonstrate leakage current values of $\approx 1 \times 10^{-9}$ A cm^{-2} at 2 MV cm^{-1}, with breakdown voltage of ≥6 MV cm^{-1} (Figure 7b), equivalent to the performance of state-of-the-art SiOC:H dielectrics.[10] Because the charge transport mechanism(s) in a-$B_xC:H_y$ films are not well understood, we cannot definitively speak to the role of methane incorporation or carbon-enrichment on leakage current; however, one possibility is that the addition of a reactive CH_4 plasma gas is able to passivate defects in the films, which would otherwise likely arise from dangling bonds created during the plasma-based film growth.

While electrical conductivity should be low for ILD applications, thermal conductivity should be high. Carbon-enriched a-$B_xC:H_y$ films were found to have slightly lower thermal conductivity values of on average 0.30 ± 0.03 W m^{-1} K^{-1} compared to values of 0.50 ± 0.04 W m^{-1} K^{-1} for moderate-density nonenriched films.[10] This value is almost identical to, if slightly higher than, those reported for SiOC:H-type dielectric films of comparable density and *k* value.[3,35–37]

3. Conclusions

Toward the development of novel interconnect dielectric materials, carbon-enriched a-$B_xC:H_y$ films were grown by PECVD from *ortho*-carborane (*o*-$C_2B_{10}H_{12}$) and methane. Key integration metrics for these films are summarized in **Table 2** alongside those for nonenriched films as well as for representative state-of-the-art SiOC:H interlayer dielectric and SiCN:H etch stop/diffusion barrier films. These carbon-enriched a-$B_xC:H_y$ films were shown to contain a significantly higher amount of extraicosahedral relative to intraicosahedral hydrocarbon than nonenriched a-$B_xC:H_y$ films via both FTIR and solid-state NMR spectroscopy. The extraicosahedral carbon was found to be in the form of sp^3 CH_2 and CH_3 species, with evidence for two types of bridging CH_2 environments, C—CH_2—C and B—CH_2—B. The carbon-enriched films were found to exhibit not only lower high-frequency dielectric constant, ε_1, but also much lower total dielectric constants, *k*—as low as 2.5—than for nonenriched films, where optimal films were obtained for low-to-moderate methane partial flow rates in the range of 5–10%. The low-*k* values were hypothesized to be due to a lower distortion/orientation ($k - \varepsilon_1$) contribution to the polarization at moderate levels of carbon enrichment, which could originate from an increase in network rigidity at low density due to the incorporation of bridging CH_2 groups. Low-density (1.1–1.2 g cm^{-3}) low-*k* carbon-enriched a-$B_xC:H_y$ films were also shown to possess a high average Young's modulus of 12 ± 3 GPa, excellent electrical properties with a low leakage current of 10^{-8}–10^{-9} A cm^{-2} at 2 MV cm^{-1} and high breakdown voltage of >6 MV cm^{-1}, and good thermal conductivity of 0.30 ± 0.03 W m^{-1} K^{-1}. Combined, these applied properties rival those of state-of-the-art

© 2017 WILEY-VCH Verlag GmbH & Co. KGaA, Weinheim

Table 2. Low-*k* dielectric properties for carbon-enriched and nonenriched a-$B_xC:H_y$ in comparison to representative state-of-the-art interlayer dielectric (ILD) and etch stop (ES)/diffusion barrier (DB) materials.

	SiOC:H	SiCN:H	BC:H	BC:H (C-enriched)
Use	ILD	ES/DB	ILD/ES/DB	ILD
Dielectric constant (*k*)	2.2–3.2	4.8–5.8	3.3 ± 0.15	2.5
Density [g cm^{-3}]	0.9–1.3	1.7–2.2	1.5 ± 0.08	1.0 ± 0.1
Pore diameter [nm]	1–1.3	0.5–0.6	≤0.7	0.7
Young's modulus [GPa]	3–15	40–100	126 ± 5	12 ± 3
Leakage current at 2 MV cm^{-1} [A cm^{-2}]	10^{-8}–10^{-9}	10^{-7}–10^{-8}	9×10^{-9} ($\pm 6 \times 10^{-9}$)	1×10^{-9}
Breakdown voltage [MV cm^{-1}]	>6	4–6	>5	>6
Thermal conductivity [W m^{-1} K^{-1}]	0.01–0.4	0.6–0.8	0.49 ± 0.04	0.31 ± 0.03
Reference	Refs. [3,7,11,37–39]	Refs. [3,40,41]	Ref. [10]	This work

SiOC:H low-*k* materials reported in the literature (Table 2). Given the suitability of a-$B_xC:H_y$ for various roles within the interconnect system, including as an etch stop or diffusion barrier,[10] as well as patterning material,[42] the ability to produce very-low-*k* materials suitable for interlayer dielectric applications sets this materials up as a flexible alternative to traditional silicon-based materials. Further, based on the demonstrated ability to control local chemical structure and enhance properties by varying precursor structure in SiOC:H, particularly in the context of carbon incorporation, we extrapolate that similar enhancements to carbon-enriched a-$B_xC:H_y$ films can be found by exploring precursor and reactive gas chemistry.

4. Experimental Section

Film Growth: Amorphous hydrogenated boron carbide (a-$B_xC:H_y$) films were grown by capacitively coupled plasma-enhanced chemical vapor deposition from a solid-state *ortho*-carborane precursor (*o*-$C_2B_{10}H_{12}$) with argon processing gas using a home-built system and process conditions as previously described in detail.[12] To incorporate additional carbon into the films, methane was added to the plasma at varying partial pressures. Argon (BIP, 99.9999%, 10 ppb O_2, 20 ppb H_2O) and methane (ultrahigh purity, 99.99%, ≤5 ppm O_2 and H_2O) gases were sourced from Airgas and flowed through additional in-line O_2/H_2O filters (<10 ppb O_2 and H_2O) prior to introduction to the chamber. *Ortho*-carborane was sourced from Katchem, and purified by sublimation in vacuo before use. To deliver the solid precursor to the plasma, argon was flowed through heated gas lines (90 °C) to a solid-state "bubbler" system (heated to 75 °C) containing *o*-carborane, and then to a mixing block (90 °C) leading into a showerhead (90 °C). Note that although the flow rate of the argon gas is known, the exact partial pressure of sublimed *o*-carborane that becomes dispersed within the carrier gas is unknown. Separately, methane was flowed directly into the mixing block, so that the combined gas mixture would be delivered to the showerhead. The partial flow rate of the methane gas, $\%CH_4$, is defined as the ratio of the methane flow rate to the total flow rate, $f_{CH4}/[f_{CH4} + f_{(Ar + o\text{-carborane})}]$, and was varied between 2.5% and 50%.

Physical Characterization: A detailed description of a majority of the measurement and analysis methods, including reproducibility studies for a subset of measurements, can be found in Nordell et al.[10,12] Unless otherwise noted, measurements were done at room temperature on films grown on silicon substrates. Briefly, atomic concentrations (%B, C, H, and O) and density were determined by nuclear reaction analysis methods.[43] Hardness (*H*) and Young's modulus (*E*) were determined by nanoindentation experiments.[44,45] Pore size was measured by PALS on selected samples.[46] FTIR spectra were acquired for films grown on Al foil with a Thermo Scientific Nicolet iS10 spectrometer using a Smart iTR attenuated total reflectance sampling accessory. NMR spectroscopy was performed on ≈20 mg samples of free-standing films isolated from Al foil using a dilute (25%) HCl solution to dissolve the substrate. Spectra were acquired with a 8.45 T magnet using a Tecmag Apollo console and home-built double-channel 4 mm wide-bore magic angle spinning (MAS) probe. Cross-polarization ^{13}C spectra were acquired with MAS spinning frequency of 8 kHz, proton RF field decoupling strength of 95 kHz, cross polarization contact time of 2 ms, and 90° pulse length of 5 µs. Adamantane was used as an external ^{13}C chemical shift reference. Thin-film thickness (*d*), index of refraction (*n*), and extinction coefficient (κ) were measured with a J.A. Woolam alpha-SE spectroscopic ellipsometer. The real part of the high-frequency (4.6×10^{14} Hz/1.96 eV) dielectric constant was calculated from the optical constants via $\varepsilon_1 = n^2 - \kappa^2$. Current–voltage (*IV*) and 100 kHz capacitance–voltage (*CV*) measurements were obtained on metal–insulator–semiconductor a-$B_xC:H_y$/Si heterostructures using a mercury probe with Keithley 2400 source meter (voltage source), 6485 picoammeter (current sensor), and 590 CV analyzer. The low-frequency (i.e., the total) dielectric constant (*k*) was determined from the *CV* curve in the accumulation region through the geometric capacitance relationship for an MIS capacitor, $k = Cd/\varepsilon_0 A$, where *d* is the sample thickness, ε_0 is the permittivity of free space, and *A* is the area of the Hg contact. Electrical resistivity (ρ) was determined from the *IV* curve in the Ohmic regime ($I \propto V^n$; $n \approx 1$) from Ohm's law, $\rho = VA/Id$. Thermal conductivity (λ) was determined using time domain thermoreflectance.[47–49]

Acknowledgements

This work was financially supported by Intel Corporation (Contract No. 2012-IN-2313). M.M.P. acknowledges funding from the Defense Threat Reduction Agency (Grant No. HDTRA1-15-1-0020). P.E.H. and J.T.G. appreciate funding from the Office of Naval Research (Grant No. N00014-15-12769).

Conflict of Interest

The authors declare no conflict of interest.

Keywords

amorphous hydrogenated boron carbide, boron carbide, carboranes, low-*k* dielectric, plasma-enhanced chemical vapor deposition

Received: March 21, 2017
Revised: August 3, 2017
Published online: September 21, 2017

[1] *Advanced Interconnects for ULSI Technology* (Eds: M. Baklanov, P. S. Ho, E. Zschech), John Wiley & Sons, Ltd, West Sussex, UK **2012**.

[2] *International Technology Roadmap for Semiconductors, Interconnect Chapter*, **2013**.

© 2017 WILEY-VCH Verlag GmbH & Co. KGaA, Weinheim

[3] S. W. King, *ECS J. Solid State Sci. Technol.* **2015**, *4*, N3029.
[4] A. Grill, *J. Vac. Sci. Technol., B.* **2016**, *34*, 20801.
[5] K. Vanstreels, C. Wu, M. R. Baklanov, *ECS J. Solid State Sci. Technol.* **2014**, *4*, N3058.
[6] I. Stassen, M. Styles, G. Grenci, H. Van Gorp, W. Vanderlinden, S. De Feyter, P. Falcaro, D. De Vos, P. Vereecken, R. Ameloot, *Nat. Mater.* **2015**, *15*, 304.
[7] D. J. Michalak, J. M. Blackwell, J. M. Torres, A. Sengupta, L. E. Kreno, J. S. Clarke, D. Pantuso, *J. Mater. Res.* **2015**, *30*, 3363.
[8] T. Frot, W. Volksen, S. Purushothaman, R. Bruce, G. Dubois, *Adv. Mater.* **2011**, *23*, 2828.
[9] L. Zhang, J.-F. de Marneffe, M. H. Heyne, S. Naumov, Y. Sun, A. Zotovich, Z. el Otell, F. Vajda, S. De Gendt, M. R. Baklanov, *ECS J. Solid State Sci. Technol.* **2014**, *4*, N3098.
[10] B. J. Nordell, T. D. Nguyen, C. L. Keck, S. Dhungana, A. N. Caruso, W. A. Lanford, J. T. Gaskins, P. E. Hopkins, D. R. Merrill, D. C. Johnson, L. L. Ross, P. Henry, S. W. King, M. M. Paquette, *Adv. Electron. Mater.* **2016**, *2*, 1600073.
[11] A. Grill, S. M. Gates, T. E. Ryan, S. V. Nguyen, D. Priyadarshini, *Appl. Phys. Rev.* **2014**, *1*, 11306.
[12] B. J. Nordell, S. Karki, T. D. Nguyen, P. Rulis, A. N. Caruso, S. S. Purohit, H. Li, S. W. King, D. Dutta, D. Gidley, W. A. Lanford, M. M. Paquette, *J. Appl. Phys.* **2015**, *118*, 35703.
[13] B. J. Nordell, C. L. Keck, T. D. Nguyen, A. N. Caruso, S. S. Purohit, W. A. Lanford, D. Dutta, D. Gidley, P. Henry, S. W. King, M. M. Paquette, *Mater. Chem. Phys.* **2016**, *173*, 268.
[14] B. D. Hatton, K. Landskron, W. J. Hunks, M. R. Bennett, D. Shukaris, D. D. Perovic, G. A. Ozin, *Mater. Today* **2006**, *9*, 22.
[15] M. S. Driver, M. M. Paquette, S. Karki, B. J. Nordell, A. N. Caruso, *J. Phys.: Condens. Matter* **2012**, *24*, 445001.
[16] M. M. Paquette, W. Li, M. S. Driver, S. Karki, A. N. Caruso, N. A. Oyler, *J. Phys.: Condens. Matter* **2011**, *23*, 435002.
[17] M. Saß, A. Annen, W. Jacob, *J. Appl. Phys.* **1997**, *82*, 1905.
[18] R. Paroli, N. Kawai, G. Lord, *Inorg. Chem.* **1989**, *28*, 1819.
[19] T. Heitz, B. Drévillon, C. Godet, J. Bourée, *Phys. Rev. B* **1998**, *58*, 13957.
[20] J. Robertson, *Mater. Sci. Eng., R* **2002**, *37*, 129.
[21] B. H. Stuart, *Infrared Spectroscopy: Fundamentals and Applications*, John Wiley & Sons, Ltd, Chichester, UK **2004**.
[22] S. W. King, M. French, J. Bielefeld, W. A. Lanford, *J. Non.-Cryst. Solids* **2011**, *357*, 2970.
[23] S. Kageyama, N. Matsuki, H. Fujiwara, *J. Appl. Phys.* **2013**, *114*, 233513.
[24] A. Grill, D. A. Neumayer, *J. Appl. Phys.* **2003**, *94*, 6697.
[25] K. Shirai, S. Emura, S. Gonda, Y. Kumashiro, *J. Appl. Phys.* **1995**, *78*, 3392.
[26] A. Annen, *Thin Solid Films* **1998**, *312*, 147.
[27] S.-H. Lin, B. J. Feldman, *Mater. Res. Soc. Symp. Proc.* **1998**, *517*, 433.
[28] G. Cho, B. K. Yen, C. A. Klug, *J. Appl. Phys.* **2008**, *104*, 13531.
[29] N. Baccile, G. Laurent, F. Babonneau, F. Fayon, M.-M. Titirici, M. Antonietti, *J. Phys. Chem. C* **2009**, *113*, 9644.
[30] K. Maex, M. R. Baklanov, D. Shamiryan, F. Lacopi, S. H. Brongersma, Z. S. Yanovitskaya, *J. Appl. Phys.* **2003**, *93*, 8793.
[31] P. A. Kohl, *Annu. Rev. Chem. Biomol. Eng.* **2011**, *2*, 379.
[32] M. F. Thorpe, D. J. Jacobs, N. V. Chubynsky, A. J. Rader, in *Rigidity Theory and Applications* (Eds: M. F. Thorpe, P. M. Duxbury), Kluwer Academic/Plenum Publishers, New York **2002**, pp. 239–277.
[33] S. W. King, J. Bielefeld, G. Xu, W. A. Lanford, Y. Matsuda, R. H. Dauskardt, N. Kim, D. Hondongwa, L. Olasov, B. Daly, G. Stan, M. Liu, D. Dutta, D. Gidley, *J. Non-Cryst. Solids* **2013**, *379*, 67.
[34] G. R. Palin, *Plastics for Engineers: An Introductory Course*, Pergamon Press, New York **1967**.
[35] J. Liu, D. Gan, C. Hu, M. Kiene, P. S. Ho, W. Volksen, R. D. Miller, *Appl. Phys. Lett.* **2002**, *81*, 4180.
[36] A. Delan, M. Rennau, S. E. Schulz, T. Gessner, *Microelectron. Eng.* **2003**, *70*, 280.
[37] M. T. Alam, R. A. Pulavarthy, J. Bielefeld, S. W. King, M. A. Haque, *J. Electron. Mater.* **2013**, *43*, 746.
[38] W. Zhou, S. Bailey, R. Sooryakumar, S. King, G. Xu, E. Mays, C. Ege, J. Bielefeld, *J. Appl. Phys.* **2011**, *110*, 43520.
[39] T. A. Pomorski, B. C. Bittel, P. M. Lenahan, E. Mays, C. Ege, J. Bielefeld, D. Michalak, S. W. King, *J. Appl. Phys.* **2014**, *115*, 234508.
[40] Y.-L. Cheng, J. Wu, T.-J. Chiu, S.-A. Chen, Y.-L. Wang, *J. Vac. Sci. Technol., B.* **2011**, *29*, 31207.
[41] S. W. King, D. Jacob, D. Vanleuven, B. Colvin, J. Kelly, M. French, J. Bielefeld, D. Dutta, M. Liu, D. Gidley, *ECS J. Solid State Sci. Technol.* **2012**, *1*, N115.
[42] S. Dhungana, T. D. Nguyen, B. J. Nordell, A. N. Caruso, M. M. Paquette, G. Chollon, W. A. Lanford, K. Scharfenberger, D. Jacob, S. W. King, *J. Vac. Sci. Technol., A* **2017**, *35*, 21510.
[43] W. A. Lanford, M. Parenti, B. J. Nordell, M. M. Paquette, A. N. Caruso, M. Mäntymäki, J. Hämäläinen, M. Ritala, K. B. Klepper, V. Miikkulainen, O. Nilsen, W. Tenhaeff, N. Dudney, D. Koh, S. K. Banerjee, E. Mays, J. Bielefeld, S. W. King, *Nucl. Instrum. Methods Phys. Res., Sect. B* **2016**, *371*, 211.
[44] Y. Lin, Y. Xiang, T. Y. Tsui, J. J. Vlassak, *Acta Mater.* **2008**, *56*, 4932.
[45] D. Koh, J.-H. Yum, S. K. Banerjee, T. W. Hudnall, C. Bielawski, W. A. Lanford, B. L. French, M. French, P. Henry, H. Li, M. Kuhn, S. W. King, *J. Vac. Sci. Technol., B.* **2014**, *32*, 03D117.
[46] D. W. Gidley, H.-G. Peng, R. S. Vallery, *Annu. Rev. Mater. Res.* **2006**, *36*, 49.
[47] D. G. Cahill, *Rev. Sci. Instrum.* **2004**, *75*, 5119.
[48] A. J. Schmidt, X. Chen, G. Chen, *Rev. Sci. Instrum.* **2008**, *79*, 114902.
[49] P. E. Hopkins, J. R. Serrano, L. M. Phinney, S. P. Kearney, T. W. Grasser, C. T. Harris, *J. Heat Transfer* **2010**, *132*, 81302.

 © 2017 WILEY-VCH Verlag GmbH & Co. KGaA, Weinheim